Computers and Fluids 256 (2023) 105838

Contents lists available at ScienceDirect

Computers and Fluids

journal homepage: www.elsevier.com/locate/compfluid

Stratified Taylor–Green vortex by lattice Boltzmann methods: Influence of stencils, forcing schemes, and collision models

Dominik Wilde [a,b,c,*], Sheel Nidhan [a], Hieu T. Pham [a], Holger Foysi [b], Dirk Reith [c,d], Sutanu Sarkar [a]

[a] Department of Mechanical and Aerospace Engineering, University of California San Diego, 9500 Gilman Drive, La Jolla, 92093, United States
[b] Department of Mechanical Engineering, University of Siegen, Paul-Bonatz-Straße 9-11, Siegen-Weidenau, 57076, Germany
[c] Institute of Technology, Resource and Energy-efficient Engineering (TREE), Bonn-Rhein-Sieg University of Applied Sciences, Grantham Allee 20, Sankt Augustin, 53757, Germany
[d] Fraunhofer Institute for Algorithms and Scientific Computing (SCAI), Schloss Birlinghoven, Sankt Augustin, 53754, Germany

ARTICLE INFO

Keywords:
Stratified flow
Lattice Boltzmann method
Taylor–Green vortex
Flux coefficient
Ocean flow
Atmosphere flow

ABSTRACT

Stably stratified Taylor–Green vortex simulations are performed by lattice Boltzmann methods (LBM) and compared to other recent works using Navier–Stokes solvers. The density variation is modeled with a separate distribution function in addition to the particle distribution function modeling the flow physics. Different stencils, forcing schemes, and collision models are tested and assessed. The overall agreement of the lattice Boltzmann solutions with reference solutions from other works is very good, even when no explicit subgrid model is used, but the quality depends on the LBM setup. Although the LBM forcing scheme is not decisive for the quality of the solution, the choice of the collision model and of the stencil are crucial for adequate solutions in underresolved conditions. The LBM simulations confirm the suppression of vertical flow motion for decreasing initial Froude numbers. To gain further insight into buoyancy effects, energy decay, dissipation rates, and flux coefficients are evaluated using the LBM model for various Froude numbers.

1. Introduction

Atmosphere and ocean currents are illustrative examples of stably stratified flows, in which the density decreases (increases) continuously with height (depth) [1]. These stable density gradients tend to suppress vertical overturning motion, leading to different turbulence physics when compared to the unstratified flows having similar configuration. Understanding stratified flows is particularly important in the fields of meteorology, oceanography, or planetary science. Yet laboratory experiments are often difficult to conduct due to the large scale separation of the flows [2]. Therefore, simulations have proven as a viable alternative.

In the past, stratified flows have been mainly studied by continuum solvers based on the Navier–Stokes equations with the Boussinesq approximation. As an alternative, the lattice Boltzmann method (LBM) [3,4] is a rapidly emerging mesoscopic fluid dynamics solver using simple stream and collide operations, being easy to implement, and well-parallelizable across CPUs and GPUs [5,6]. Recent work has shown that the LBM shows at least similar performance as highly-tuned finite-difference Navier–Stokes solvers for weak compressible approaches [7], indicating no disadvantage from a performance point of view. In addition, LBM simulations have proven to be both efficient and accurate for wall-bounded turbulent flow simulations when equipped with a suitable grid refinement [8]. In the future, the use of the LBM may also be beneficial for wall-bounded, stably stratified flow simulations, but before that, the method should be thoroughly evaluated.

The LBM has made considerable progress in the prediction of buoyancy-driven flows [9,10], shown, for example, in simulations of Rayleigh–Bénard flows by Shan [11], Lohse and Toschi [12], Calzavarini et al. [13], Kao and Yang [14], as well as Frapolli et al. [15]. Besides these studies in which the turbulence is triggered by unstable stratification, the performance of LBM in simulating stably stratified turbulence has not been explored in depth. In two dimensions, Biferale et al. pioneered the study of stably stratified flow in Rayleigh–Taylor systems using the LBM [16]. Beyond that, the few available works using the LBM include the work by Wang et al. [17], who found good agreement between the multi-relaxation LBM and a large-eddy simulation (LES) using finite-difference method when they simulated a 3D stratified atmospheric boundary layer over a ridge. It is of interest to expand their study by comparing LBM with the direct numerical simulation (DNS) method, in which there is no effect of subgrid parameterization.

* Corresponding author at: Department of Mechanical Engineering, University of Siegen, Paul-Bonatz-Straße 9-11, Siegen-Weidenau, 57076, Germany.
E-mail address: wilde.aerospace@gmail.com (D. Wilde).

https://doi.org/10.1016/j.compfluid.2023.105838
Received 5 September 2022; Received in revised form 29 January 2023; Accepted 21 February 2023
Available online 28 February 2023

Recently, Feng et al. proposed a hybrid model for atmospheric convection [18]. Their work used the LBM for the momentum equation, while the temperature field was directly solved through a finite-volume approach. By contrast, most other approaches discretize both equations with the LBM. The optimal way to discretize coupled Navier–Stokes and advection–diffusion systems with the LBM was recently explored by Dapelo et al. [19]. The authors found that a coupled LBM-LBM for both the Navier–Stokes and advection–diffusion equation is suitable, provided that the diffusivity of the flow is not too small. That said, detailed analyses of LBM simulations of stably stratified turbulence are largely missing. To fill this gap, a suitable lattice Boltzmann framework has been developed in this work to execute three-dimensional, stratified Taylor–Green vortex simulations.

The three-dimensional Taylor–Green vortex [20] has been extensively used for incompressible flow simulations to scrutinize algorithms in terms of numerical dissipation and stability [21–24]. The flow involves simple initial conditions which make it a preferred test case in comparative studies of different numerical methods. In recent years, the test case has also been extended to supersonic [25–27] and stratified flow [28–30], revealing new flow physics. In the unstratified case, the few initial modes of the Taylor–Green vortex ultimately turn into nearly homogeneous turbulence. Contrary to that, mixing in the stratified Taylor–Green vortex mostly occurs along the horizontal planes, whereas the buoyancy force suppresses vertical motions [30]. In this study, we chose Taylor–Green vortex as the test case to explore the ability of LBM in capturing the evolution of stratified turbulent flows.

This article describes a lattice Boltzmann model for the simulation of three-dimensional stably stratified Taylor–Green vortices. It explores the performance of the solver by the established measures of the stratified Taylor–Green vortex such as kinetic and potential energy, dissipation rates, buoyancy Reynolds number, flux coefficients, and kinetic energy spectrum. To further tune the solver towards optimal results, simulations with different stencils, forcing schemes, and collision models are executed, evaluated, and documented in this manuscript.

The article is organized as follows. The next section describes the methodology including the governing equations and the LBM model. Besides, the section also provides the initial conditions and parameters of the Taylor–Green vortex. Thereafter, Section 3 compiles the results and the article ends with a conclusion.

2. Methodology

The incompressible Navier–Stokes equations with Boussinesq approximation for velocity u_α read in index notation

$$\partial_\alpha u_\alpha = 0 \tag{1}$$

$$\partial_t u_\alpha + u_\beta \partial_\beta u_\alpha = -\partial_\alpha p - \rho' G e_z + \nu \partial_\beta \partial_\beta u_\alpha. \tag{2}$$

Here, p denotes pressure, G is gravity, ν is the kinematic viscosity. The density variation ρ' is part of the total density

$$\rho(x, y, z, t) = \rho_0 + \rho_b(z) + \rho'(x, y, z, t). \tag{3}$$

Besides ρ', it consists of the constant reference density ρ_0 and the background density $\rho_b(z)$ which linearly decreases with height z.

The density variation evolves over time by

$$\partial_t \rho' + \partial_\alpha(\rho' u_\alpha) = -u_z \frac{\partial \rho_b}{\partial z} + \tilde{D} \partial_\alpha \partial_\alpha \rho', \tag{4}$$

where $\tilde{D}$ stands for the mass diffusivity.

2.1. Approximation of the momentum equation

A coupled lattice Boltzmann model with two distribution functions is used to approximate Eqs. (1) through (4). The lattice Boltzmann equation describes the dynamics of the discrete particle distribution function f_i and reads

$$f_i\left(\boldsymbol{x} + \boldsymbol{c}_i \delta_t, t + \delta_t\right) = f_i(\boldsymbol{x}, t) + \Omega_i^f + F_i, \tag{5}$$

where i is the index of the respective discrete velocity $\boldsymbol{c}_i$, δ_t is the time step size, Ω_i^f is a collision operator, and F_i is a discrete forcing term which is computed from the local force $\hat{\boldsymbol{F}}$. The moments of f_i yield the density $\hat{\rho}$ and the velocity $\boldsymbol{u}$

$$\hat{\rho}(\mathbf{x}, t) = \sum_i f_i(\mathbf{x}, t), \tag{6}$$

$$\mathbf{u}(\mathbf{x}, t) = \frac{1}{\hat{\rho}} \sum_i \mathbf{c}_i f_i(\mathbf{x}, t) + \frac{\hat{\boldsymbol{F}} \delta_t}{2\hat{\rho}}. \tag{7}$$

The Bhatnagar–Gross–Krook collision model [31] is a common choice to express the collision operator

$$\Omega_i^f = -\frac{1}{\tau_f}\left(f_i - f_i^{\mathrm{eq}}\right), \tag{8}$$

with the dimensionless relaxation parameter $\tau = \nu/c_s^2 + 0.5$, where c_s is the lattice speed of sound and the term of 0.5 results from the time integration of the collision operator [5,32]. Eq. (8) assumes that the particle distribution functions relax according to τ towards the equilibrium distribution function

$$f_i^{\mathrm{eq}}(\hat{\rho}, \boldsymbol{u}) = \hat{\rho} \Theta_i^{\mathrm{eq}}(\boldsymbol{u}) \tag{9}$$

with the second-order Hermite expansion of the Maxwell–Boltzmann distribution

$$\Theta_i^{\mathrm{eq}}(\mathbf{u}) = w_i \left(1 + \frac{u_\alpha c_{i\alpha}}{c_s^2} + \frac{\left(u_\alpha c_{i\alpha}\right)^2}{2c_s^4} - \frac{u_\alpha u_\alpha}{2c_s^2}\right), \tag{10}$$

where w_i are the quadrature weights.

The force term F_i can be handled in different ways, of which we have chosen three schemes to study. Primarily, this work uses the Shan–Chen forcing scheme [33], unless otherwise stated. This forcing scheme avoids prescribing a forcing term explicitly and therefore results in $F_i = 0$ in Eq. (5). Instead, the force is incorporated into the velocity $\boldsymbol{u}$ that enters the equilibrium (10)

$$\mathbf{u}^{\mathrm{eq}}(\mathbf{x}, t) = \frac{1}{\hat{\rho}} \sum_i \mathbf{c}_i f_i(\mathbf{x}, t) + \frac{\hat{\boldsymbol{F}} \tau_f}{2\hat{\rho}}, \tag{11}$$

in lieu of Eq. (7). The other two forcing schemes used in this article are from Kupershtokh et al. [34] and from Guo et al. [35]. For a more detailed analysis and description of the forcing schemes, we refer to the article by Huang et al. [36], which reviews different forcing schemes in the LBM.

2.2. Approximation of the advection–diffusion equation

For the advection–diffusion Eq. (4) of the density variation ρ', an equation for the distribution function g_i is added

$$g_i\left(\boldsymbol{x} + \boldsymbol{c}_i \delta_t, t + \delta_t\right) = g_i(\boldsymbol{x}, t) + \Omega_i^g + S_i, \tag{12}$$

where S_i models the source term in Eq. (4). It depends on the local vertical velocity u_z and is given by

$$S_i = w_i \left(u_z \frac{\partial \rho_b}{\partial z}\right)_{LB}. \tag{13}$$

The subscript LB indicates that both the vertical velocity u_z and the background density gradient $\left(\frac{\partial \rho_b}{\partial z}\right)$ need to be in lattice units with the conversion factor

$$\left(\frac{\partial \rho_b}{\partial z}\right)_{\mathrm{LB}} = \left(\frac{\partial \rho_b}{\partial z}\right) \delta_x, \tag{14}$$

depending on the grid size δ_x.

The collision operator of g_i is similar to the counterpart of f_i in Eq. (8)

$$\Omega_i^g = -\frac{1}{\tau_g}\left(g_i - g_i^{\mathrm{eq}}\right), \tag{15}$$

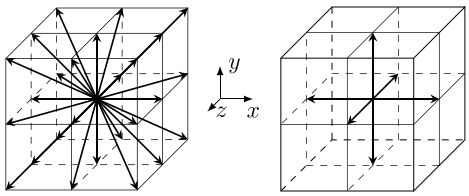

Fig. 1. Left: D3Q27 stencil. Right: D3Q7 stencil.

however, the relaxation parameter is linked to the thermal diffusivity $\tilde{D}$, i.e., $\tau_g = \tilde{D}/c_s^2 + 0.5$. The equilibrium g_i^{eq} is determined by

$$g_i^{\mathrm{eq}}(\rho', \boldsymbol{u}) = (\rho' + \rho_\infty)\Theta_i^{\mathrm{eq}}(\boldsymbol{u}). \tag{16}$$

The computational effort to determine Eq. (16) is reduced whenever the stencils of f_i and g_i coincide, however, different stencils for both equations can be chosen as mentioned briefly below. In the case that the stencils for f_i and g_i differ, the term Θ_i in Eq. (10) needs to be computed separately for f_i^{eq} and g_i^{eq}. The density variation is principally determined by the moment

$$\rho'(\boldsymbol{x}, t) = \sum_i g_i(\boldsymbol{x}, t) - \rho_0, \tag{17}$$

however, for the calculation of the equilibrium (16), a modified expression has to be used to minimize discretization errors [5]

$$\rho'(\boldsymbol{x}, t) = \sum_i g_i(\boldsymbol{x}, t) + \frac{R_i}{2} - \rho_0, \tag{18}$$

$$R_i = \left(1 - \frac{1}{2\tau_g}\right) S_i. \tag{19}$$

The density variation ρ' determines the local force $\hat{\boldsymbol{F}}$ through the Boussinesq approximation

$$\hat{\boldsymbol{F}} = \begin{pmatrix} 0 \\ 0 \\ -G\rho' \end{pmatrix}, \tag{20}$$

with gravity G.

Technically, the system is equipped with two independent expressions for the densities: the density $\hat{\rho}$ appearing in Eq. (6) models the pressure variation $p' = c_s^2\hat{\rho}$, whereas the density variation ρ' evolves through Eq. (12). Since compression work and viscous heating are negligible for the explored flows, this division into two variables is justified [5].

2.3. Stencils

A particular set of discrete velocities $\mathbf{c}_i$ is called velocity set or stencil. It dictates how the particle distribution functions f_i and g_i move through the domain during the streaming step. For the momentum equation the most common choices are the D3Q19 and D3Q27 stencil, whereas the advection–diffusion equation is often solved by the much smaller stencil D3Q7 [5]. Generally, the computational effort of the LBM scales linearly with the number of discrete velocities, favoring smaller stencils. However, the stencils differ not only in the number of discrete velocities, but also in the underlying velocity space discretization [37,38]. Thus, different stencils might exhibit differences in accuracy, but for stably stratified flow it is unclear to what extent. Therefore, this article examines differences in terms of accuracy for the most common stencils to discretize the momentum and the advection–diffusion equation. The stencils D3Q19 and D3Q27 were used for the momentum equation, and the stencils D3Q7, D3Q19, and D3Q27 were employed in the advection–diffusion equation. Fig. 1 depicts the stencils D3Q27 and D3Q7. In addition, Table A.1 lists all stencils' discrete velocities, weights, and lattice speeds of sound.

Throughout the article, the notation D3Q27×α will be used, with α indicating the number of discrete velocities used for g_i. In the example of Fig. 1 we would use D3Q27×7, showing that a 3D stencil with 27 discrete velocities was used for the distribution function f_i, while the second grid g_i employed seven velocities.

2.4. Entropic multi-relaxation time collision operator

It is known that the customary BGK collision operator is prone to instabilities in underresolved, turbulent simulations [39,40]. Therefore, alternative collision models have been proposed, which trade accuracy against stability [4]. The entropic multi-relaxation time collision operator by Karlin–Bösch–Chikatamarla *KBC* is a prominent proposal [41] using adaptively determined relaxation rates. In the KBC model, the distribution function f_i is split into the contributions of the conserved moments k_i, the shear moments s_i, and the higher-order moments h_i, i.e.,

$$f_i = k_i + s_i + h_i. \tag{21}$$

Then, each of the non-conservative groups relaxes individually to its individual equilibrium, s_i^{eq} and h_i^{eq}, according to

$$\Omega_i^{\mathrm{f,KBC}} = -\frac{1}{\tau}(s_i - s_i^{\mathrm{eq}} + \frac{\gamma}{2}(h_i - h_i^{\mathrm{eq}})). \tag{22}$$

The relaxation parameter γ is determined afresh for every time step and grid point by minimizing an entropy function during the collision step. Both procedures to split k_i, s_i, and h_i from f_i as well as to find γ can be found in the work by Bösch et al. [42].

In the present work, usually the BGK model is used for both f_i and g_i. For results shown later using the KBC model, it is only applied to f_i, whereas g_i still relaxes using the BGK model in Eq. (15). An extension of the KBC model to the second distribution function g_i has been proposed by Morrison et al. [43], but is not used here.

2.5. Stratified 3D Taylor–Green vortex

The stratified three-dimensional Taylor–Green vortex is a slightly modified version of the original unstratified test case by Brachet et al. [44]. The stratified case has been extensively studied by Remmler and Hickel [28] as well as Jadhav and Chandy [30].

Three dimensionless numbers characterize this flow, the Reynolds, Froude, and Schmidt number. The Reynolds number is defined here as $\mathrm{Re}_0 = UL/\nu$, with characteristic velocity $U = 1$ and characteristic length $L = 1$. It is set to $\mathrm{Re}_0 = 1600$ in all simulations. By contrast, the Froude number is defined as $\mathrm{Fr}_0 = U/(NL)$ and it depends on the buoyancy frequency

$$N = \sqrt{-\frac{G}{\rho_0}\frac{\partial \rho_b}{\partial z}}. \tag{23}$$

Except for Section 3.4, where the results with different Froude numbers will be compared, the Froude number was set to $\mathrm{Fr}_0 = 1$.

The third dimensionless number, the Schmidt number, is the ratio of kinematic viscosity and mass diffusivity and is set to $\mathrm{Sc} = \nu/\tilde{D} = 0.7$.

The initial velocity and pressure fields in the domain $V \in [0, 2\pi]^3$ are

$$\boldsymbol{u}(\boldsymbol{x}, t = 0) = U \begin{pmatrix} \sin(x)\cos(y)\cos(z) \\ -\cos(x)\sin(y)\cos(z) \\ 0 \end{pmatrix}, \tag{24}$$

$$p(\boldsymbol{x}, t = 0) = \frac{1}{16}(\cos(2x) + \cos(2y))\cos(2z + 2), \tag{25}$$

whereas the initial density variation is set to

$$\rho'(\boldsymbol{x}, t = 0) = 0. \tag{26}$$

The time t is expressed by the characteristic time $t_c = L/U = 1$. The Mach number $\mathrm{Ma} = U_{\mathrm{LB}}/c_s$ relates the characteristic lattice velocity

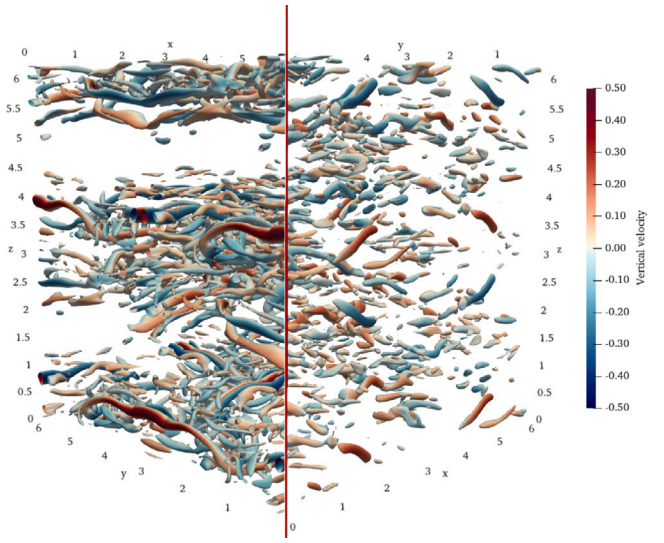

Fig. 2. Isocontour of the Q-criterion $Q = 1.5$ at $t = 15$, colored by vertical velocity u_z. The cubical domain is split in half to depict the difference of the influence of Fr_0. Left half: $\mathrm{Fr}_0 = 1.0$; right half: $\mathrm{Fr}_0 = \infty$.

U_{LB} and the lattice speed of sound c_s. In weakly compressible flow simulations, Ma serves as a numerical parameter which scales with the time step size of the simulation. Here, the initial Mach number is set to Ma = 0.1, i.e., $U_{\mathrm{LB}} = 0.0577$, which enters Eq. (24) for the actual simulation.

The simulations were conducted using the lattice Boltzmann solver *Lettuce*, which is written in Python and utilizes the PyTorch machine learning framework. It is able to perform simulations on GPUs, and can be run on a local laptop using an Nvidia RTX 3070 GPU with 8 GB of RAM for simulations with $N_g = 128^3$ or fewer grid points. These simulations with single precision and with D3Q27x7 take about 13 min to reach simulation time $t = 30$, with 29 million lattice updates per second. For simulations with $N_g = 256^3$ grid points, a more powerful Nvidia Tesla V100 GPU on the OMNI compute cluster at the University of Siegen was used, taking about 80 min, with 72.5 million lattice updates per second. It is important to note that the Lettuce code is not currently optimized for speed, so future optimization of the collision and streaming steps could result in a significant increase in computation speed [45].

3. Results

To get a first impression of the stratification effects on the Taylor–Green vortex, Fig. 2 depicts the isocontour of the Q-criterion $Q = 1.5$ at $t = 15$ within the cubical domain for $\mathrm{Fr}_0 = 1.0$ on the left and for the unstratified case on the right, i.e., $\mathrm{Fr}_0 = \infty$. The vertical velocity is described by the color of the isocontours. The figure reveals, how the buoyancy force effectively hinders the flow to reach a homogeneous state for $\mathrm{Fr}_0 = 1$. Instead, the flow mainly mixes in the horizontal directions, leading to notable layering in the vertical direction. By contrast, the flow of the unstratified case can spread unhindered in the vertical direction.

3.1. Kinetic and potential energy

The total energy $E_{\mathrm{tot}} = E_{\mathrm{k}} + E_{\mathrm{p}}$ of the stratified Taylor–Green vortex flow consists of the kinetic energy

$$E_{\mathrm{k}} = \frac{1}{(2\pi)^3} \int_V \frac{1}{2} |\boldsymbol{u}|^2 \, dV, \tag{27}$$

and potential energy

$$E_{\mathrm{p}} = \frac{1}{(2\pi)^3} \int_V \frac{1}{2} \left(\frac{G}{N} \frac{\rho'}{\rho_0} \right)^2 dV. \tag{28}$$

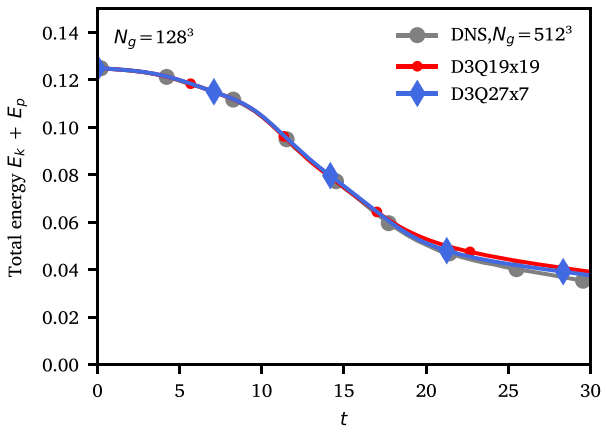

Fig. 3. Evolution of the total energy $E_{\mathrm{k}} + E_{\mathrm{p}}$ over time for two LBM configurations. The total energy consists of the kinetic energy shown in Fig. 4 and the potential energy shown in Fig. 5. DNS from [30].

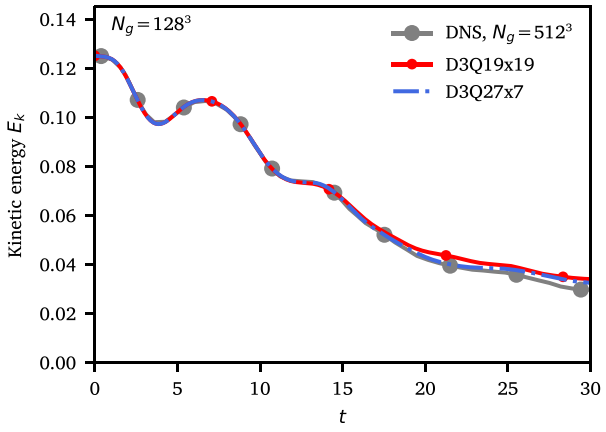

Fig. 4. Evolution of the kinetic energy E_{k} over time for two LBM configurations. DNS from [30].

Fig. 3 shows the decay of the total energy at a resolution of $N_g = 128^3$ for the stencil configurations D3Q27x7 and D3Q19x19. Apparently, both curves coincide well with the DNS reference solution at $N_g = 512^3$, which is taken from Jadhav and Chandy [30]. However, towards the end of the simulations, the plots slightly deviate, with a larger deviation for the D3Q19x19 case.

This difference is also observed for the components of E_{tot}. Fig. 4 shows how the kinetic energy periodically fluctuates over time due to the buoyancy force, although the overall decay is apparent. The good agreement of the LBM solution to the reference is confirmed, but Fig. 4 also reveals some deviations at the end of the simulation.

The potential energy E_{p} depicted in Fig. 5 shows the initial energy transfer from kinetic to potential energy shortly after the begin of the simulation, which is accurately captured by the LBM. At the second peak, an overshoot of the potential energy is observed, with larger deviations for the D3Q27x7 stencil beginning from $t \approx 15$. For higher resolutions, such as $N_g = 256^3$, the potential energy is nearly perfectly captured with the D3Q27x7 configuration, which can be seen from Fig. 6. It is worth noting that for a lower resolution of $N_g = 64^3$ the simulation is unstable when using D3Q27x7.

3.2. Dissipation of kinetic and potential energy

Next, the dissipation was explored by two different measures. The first measure is the decay of the total energy $-dE_{\mathrm{tot}}/dt$, where the temporal derivative of E_{tot} is obtained by central finite differences of

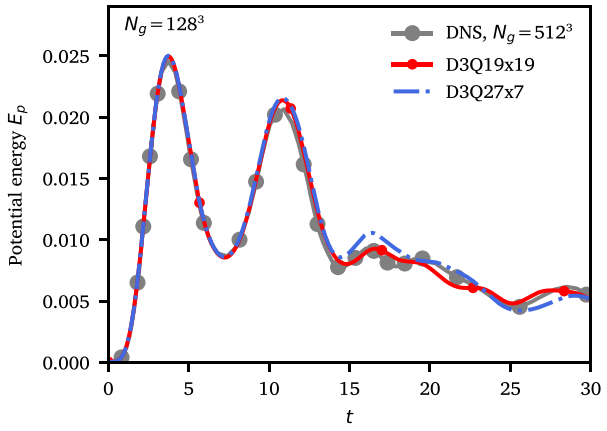

Fig. 5. Evolution of the potential energy E_p over time for two LBM configurations. DNS from [30].

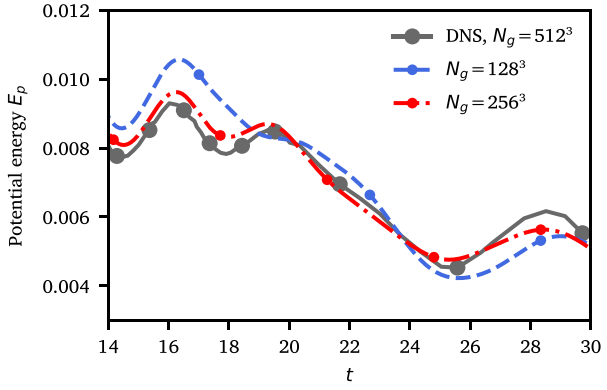

Fig. 6. Comparison of the potential energy E_p towards the end of the simulation for resolutions $N_g \in [128^3, 256^3]$ with D3Q27x7. DNS from [30].

second order. This observable considers both physical and numerical dissipation in the system. The results are shown in Fig. 7 with different stencils and resolutions. At a very low resolution $N_g = 64^3$, the D3Q19x19 simulation is stable, but the deviations from the reference from Jadhav and Chandy [30] are significant. By contrast, the $N_g = 64^3$ simulation with D3Q27x7 was unstable, which indicates that this stencil configuration is probably not the best choice in strongly underresolved simulations. Nevertheless, at a resolution of $N_g = 128^3$, the configuration D3Q27x7 accurately reproduces the kinetic energy decay, with only small deviations from the reference. This also applies to the D3Q19x19 run, but the discrepancies are more visible during the second half of the simulation. At $N_g = 256^3$, the dissipation of D3Q27x7 practically coincides with the reference.

The second measure, besides $-dE_{\text{tot}}/dt$, is the total dissipation with respect to the resolved scales $\varepsilon_{\text{tot}} = \varepsilon_k + \varepsilon_p$, which consists of the dissipation of the kinetic energy

$$\varepsilon_k = \frac{\nu}{(2\pi)^3} \int_V (\nabla \times \mathbf{u})^2 \, dV, \tag{29}$$

and the dissipation of the potential energy

$$\varepsilon_p = \frac{\tilde{D}}{(2\pi)^3} \int_V \left(\frac{G}{N} \frac{\nabla \rho'}{\rho_0} \right)^2 dV. \tag{30}$$

In contrast to the decay of the total energy $-dE_{\text{tot}}/dt$, this measure does not include numerical dissipation. Instead, the measures serve as an indicator for how accurately the gradients of velocity and density variation are represented in the simulation.

The resolution study of the temporal evolution of $\varepsilon_k + \varepsilon_p$ can be found in Fig. 8 for D3Q27x7. It depicts that the agreement to the reference is remarkable even at $N_g = 128^3$. When choosing an inappropriate low resolution, however, the values of the reference will not be reproduced qualitatively. This undesired behavior is demonstrated based on the resolution $N_g = 104^3$. This unusual resolution was selected to produce only minimal deviations from the reference, while smaller resolutions yield even more significant inaccuracies.

Next, we compared the performance of different stencil configurations in terms of the dissipation. Fig. 9 contrasts the total dissipation among the stencils at the low resolution $N_g = 64^3$. Here, the reference solution [30] is clearly missed by all configurations. In particular, the D3Q27x7 configuration overestimates the dissipation rate before the simulation runs unstable. For two other configurations, D3Q19x19 and D3Q27x27, the results are still comparable to the dynamic Smagorinsky model that was used by Jadhav and Chandy at the same resolution [30].

Next, the resolution was doubled per direction to $N_g = 128^3$. The results in Fig. 10(a) and (b) show that the dissipation of the filtered DNS [30] is nearly perfectly captured by the D3Q27x7 configuration. By contrast, all configurations with more than seven discrete velocities for g_i underestimate the total dissipation.

The differences in the total dissipation rate can be partly explained when evaluating the dissipation of the kinetic and potential energy individually, which are both depicted in Fig. 11 for $N_g = 128^3$ and $N_g = 256^3$. While the kinetic energy dissipation with $N_g = 128^3$ is underestimated by the solver in comparison to $N_g = 256^3$, the potential energy dissipation is overestimated by the $N_g = 128^3$ simulation. This indicates that at the lower resolution $N_g = 128^3$, the resolved fraction of the flow does not dissipate sufficient kinetic energy. However, this gap of dissipation is partly compensated by the larger potential energy dissipation ε_p.

3.3. Buoyancy Reynolds number

Another measure to quantify turbulent mixing in stratified flows is the buoyancy Reynolds number

$$\text{Re}_b = \frac{\varepsilon_k}{\nu N^2}. \tag{31}$$

Similar to the dissipation, the buoyancy Reynolds number shows a double peak around $t = 15$, which needs to be reproduced by the solver. The temporal evolution of the buoyancy Reynolds number Re_b is shown in Fig. 12, demonstrating that a resolution of $N_g = 256^3$ is needed to reproduce all stratification effects correctly, but that a lower resolution $N_g = 128^3$ also provides qualitatively meaningful results. On the contrary, the simulations with $N_g = 64^3$ do not yield reliable values of Re_b at all.

3.4. Froude number effects

The initial Froude number Fr_0 is the relevant dimensionless number to characterize the degree of stratification of the flow. Fig. 13(a) illustrates the effects of different Froude numbers for the Taylor–Green vortex flow on the basis of the kinetic energy, while Fig. 13(b) does the same for the potential energy. On the one hand, lower Froude number such as $\text{Fr}_0 = \{0.16, 0.33, 0.5\}$ implicate strong stratification. For the smallest Froude numbers $\text{Fr}_0 = 0.16$ and $\text{Fr}_0 = 0.33$, the flow is viscosity-affected [28], and the decay of the kinetic energy in Fig. 13(a) is decelerated with respect to the unstratified case $\text{Fr} = \infty$. For comparison, Fig. 13 (a) also includes the unstratified case $\text{Fr}_0 = \infty$, where accordingly no conversion of kinetic and potential energy takes place. On the other hand, at a higher Froude number of $\text{Fr}_0 = 2.0$, stratification leads to a faster dissipation of kinetic energy. Thus, a large amount of kinetic energy is initially converted into potential energy, which is shown in Fig. 13(b). Fig. 13 shows that the frequency of the oscillatory exchange between kinetic and potential energy increases as Fr decreases and, furthermore, the frequency is $2N$. The dissipation of kinetic energy ε_k and dissipation of potential energy ε_p are displayed in Figs. 14(a) and 14(b). Firstly, the figures show that the time of the

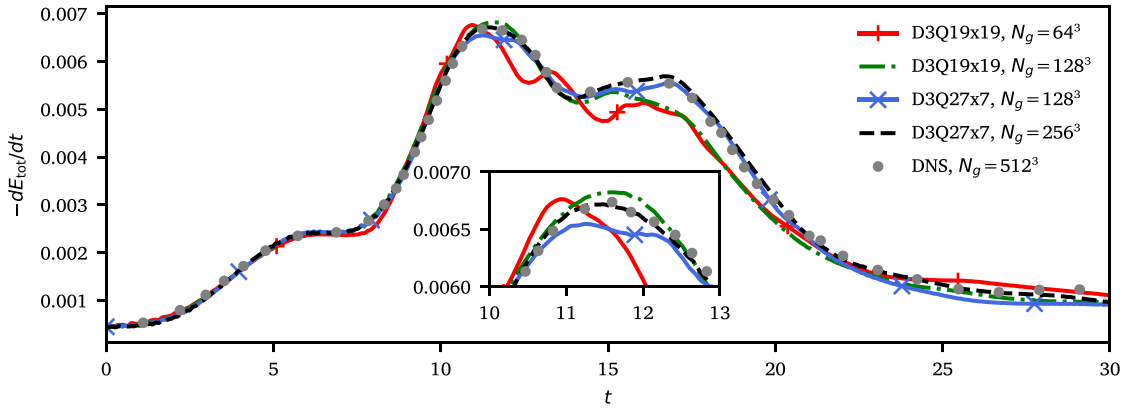

Fig. 7. Total energy decay over time with different stencils and resolutions. DNS from [30].

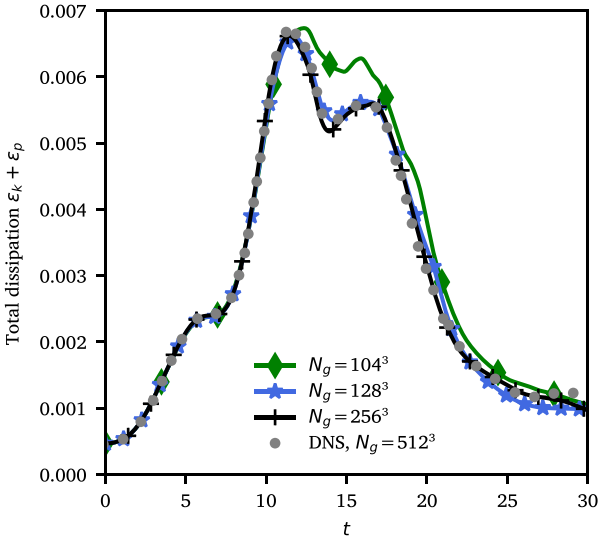

Fig. 8. Total dissipation over time using D3Q27x7. DNS from [30].

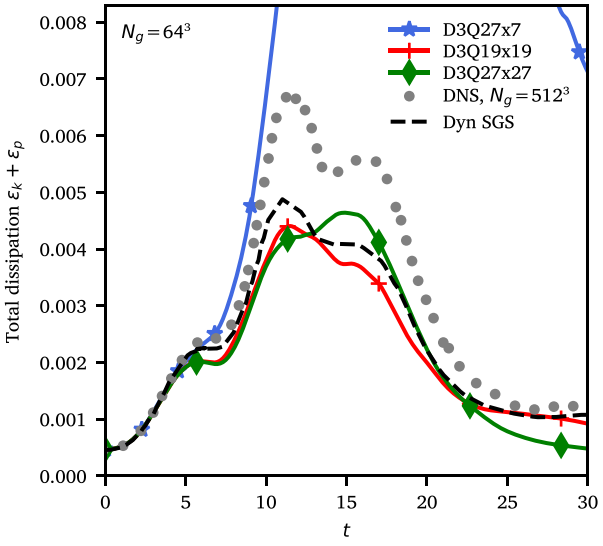

Fig. 9. Total resolved dissipation over time at resolution $N_g = 64^3$. DNS and dynamic SGS model by Jadhav and Chandy [30].

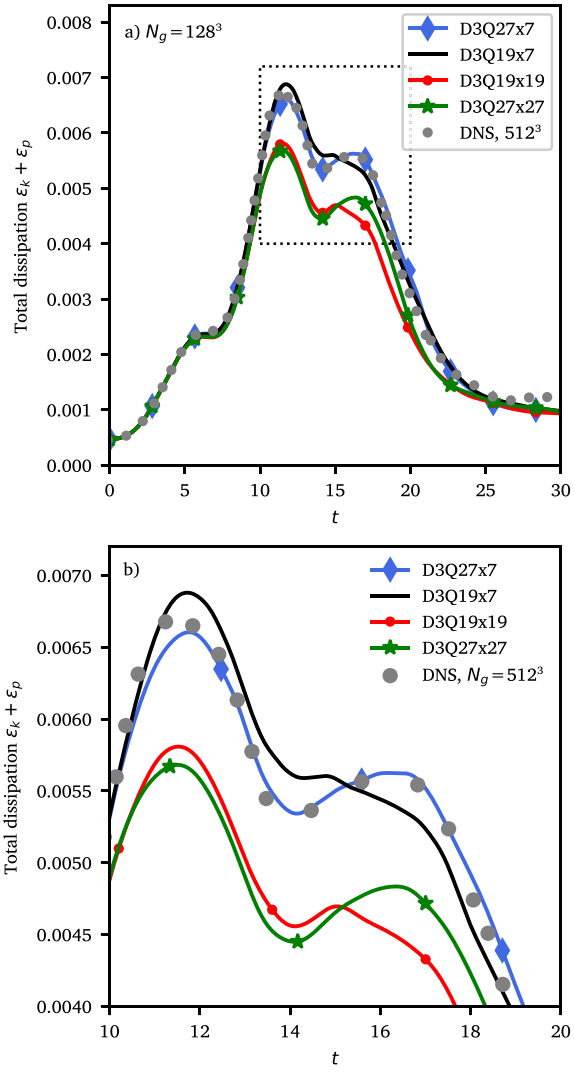

Fig. 10. (a) Total resolved dissipation over time at resolution $N_g = 128^3$. DNS by Jadhav and Chandy [30]. The area within dotted rectangle is shown in (b).

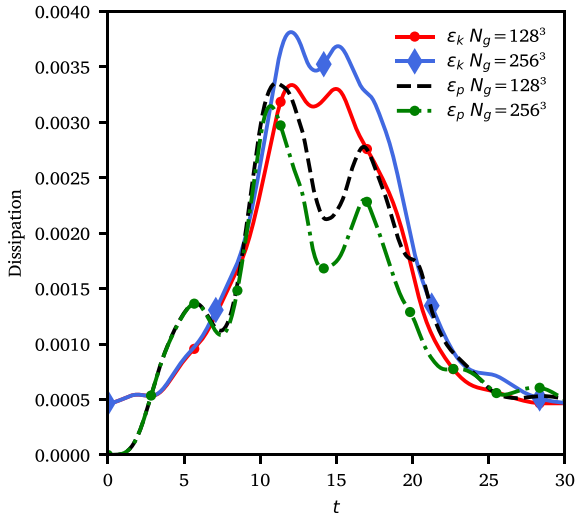

Fig. 11. Dissipation of the kinetic energy ε_k and potential energy ε_p of D3Q27x7 for the resolutions $N_g = 128^3$ and $N_g = 256^3$, respectively.

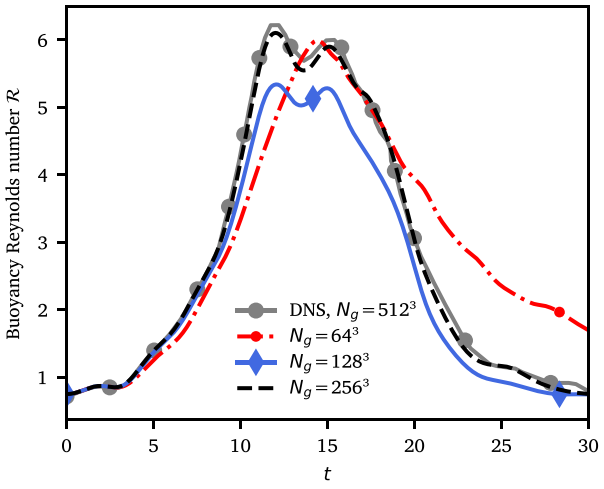

Fig. 12. Buoyancy Reynolds number Re_b over time for D3Q27x7 for initial Froude number $\mathrm{Fr}_0 = 1$. DNS from Jadhav and Chandy [30].

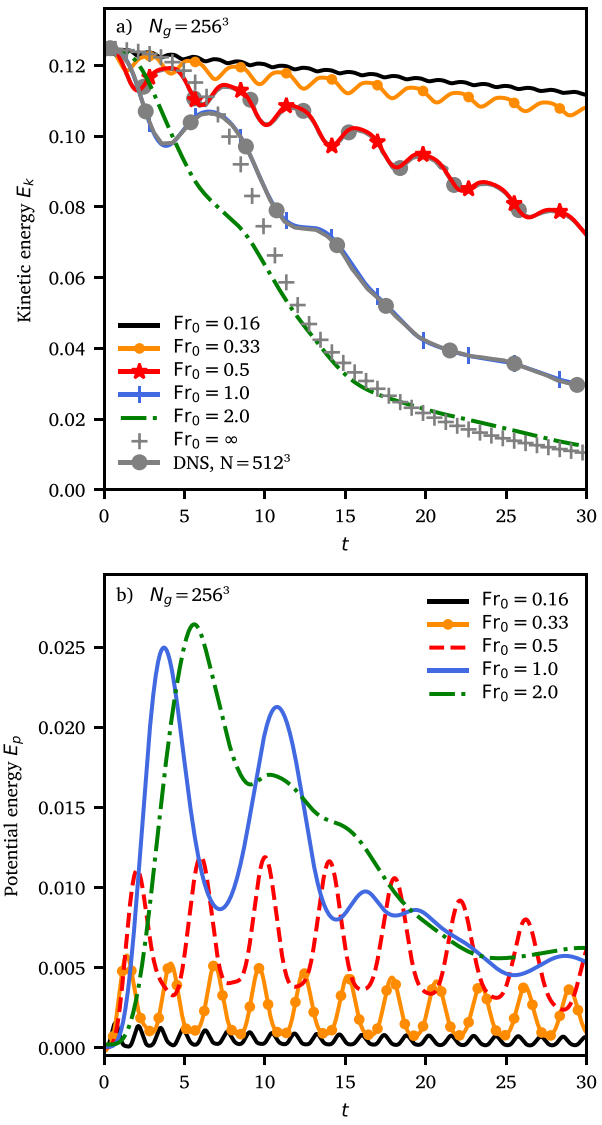

Fig. 13. Kinetic energy (a) and potential energy (b) over time for different Froude numbers at resolution $N_g = 256^3$ using the D3Q27x7 stencils.

dissipation peak depends on the Froude number, where large Froude numbers lead to earlier peaks. However, the peak time can be different for ε_k and ε_p, as the simulation with $\mathrm{Fr} = 2.0$ clearly reveals. Secondly, the peak values of ε_k and ε_p scale with the Froude number, i.e., small Froude numbers yield small dissipation maxima.

In oceanography, the flux coefficient $\Gamma = \varepsilon_p/\varepsilon_k$ is an important parameter to quantify the mixing processes in stratified shear flows [46–49]. This motivates Fig. 15, which shows the flux coefficient Γ over time for different Froude numbers. In essence, Fig. 15 confirms the previous observations that the strongly stratified test cases with low Froude numbers $\mathrm{Fr}_0 = \{0.16, 0.33\}$ are dominated by the dissipation of the kinetic energy ε_k during the entire simulation. This finding manifests in small Γ values at small Froude numbers. For larger Froude numbers $\mathrm{Fr}_0 = \{1.0, 2.0\}$, the dissipation of the potential energy ε_p initially dominates, leading to larger flux coefficient values. At intermediate time, the flux coefficient decreases before slightly increasing again towards the end of the simulation.

Next, the flux coefficient of the bulk Γ_b is computed by dividing the time-integrated values of ε_p by the time-integrated values of ε_k, i.e.,

$$\Gamma_b = \frac{\int_0^{30} \varepsilon_p dt}{\int_0^{30} \varepsilon_k dt}. \tag{32}$$

The bulk flux coefficient Γ_b is displayed in Fig. 16 over the Froude number Fr_t for different initial Froude numbers Fr_0. The turbulent Froude number Fr_t represents the ratio of the inertial forces to the buoyancy forces in the bulk and is defined as

$$\mathrm{Fr}_t = \frac{\int_0^{30} \epsilon_k dt}{N \int_0^{30} E_k dt}. \tag{33}$$

Fig. 16 demonstrates that the time-integrated turbulent Froude number Fr_t increases with increasing initial Froude number Fr_0. The figure also shows that, while Γ_b is related to Fr_t, it does not grow without bounds and follows a nonlinear relationship. In particular, the value of Γ_b appears to converge towards $\Gamma_b \approx 0.8$ for the present Taylor–Green vortex test case.

The distribution of the kinetic energy over the wavenumbers k of the Taylor–Green vortex can be seen in the spectrum in Fig. 17, obtained at $t = 15$. At this time, the unstratified Taylor–Green vortex flow has already transported a large amount of kinetic energy from the large scales to the small scales, where it is finally dissipated. The more stratified the flow, however, the larger the energy that is still contained in the large scales at $t = 15$. Fig. 18 visualizes the effect of different

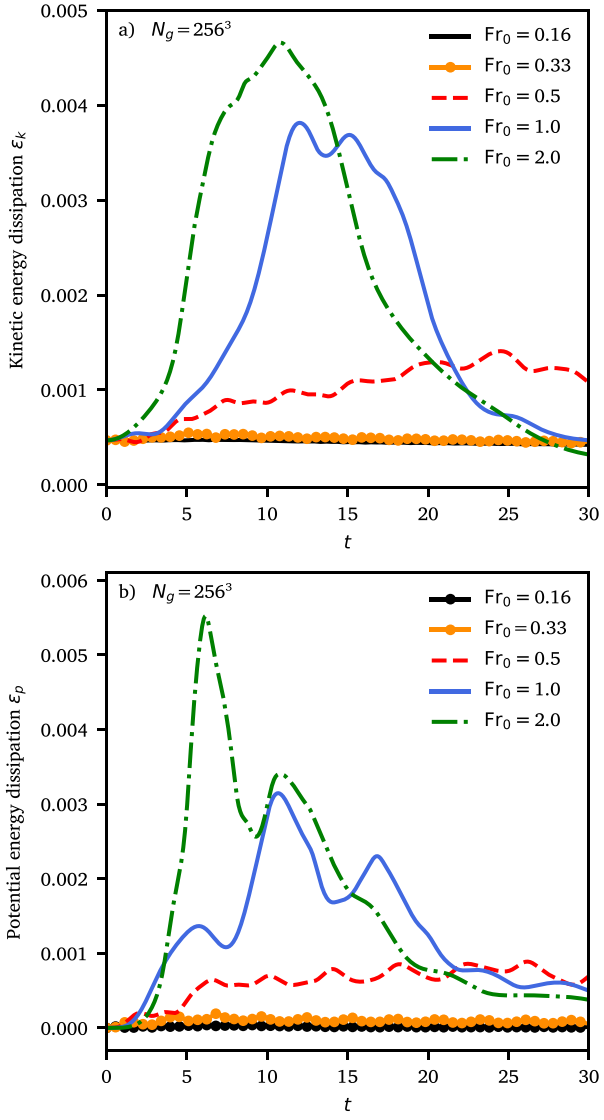

Fig. 14. Kinetic energy dissipation (a) and potential energy dissipation (b) over time for different Froude numbers at resolution $N_g = 256^3$ using the D3Q27x7 stencils.

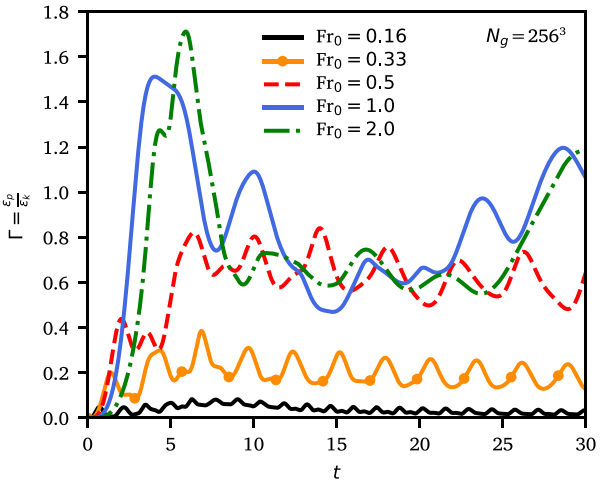

Fig. 15. Flux coefficient Γ over time for different Froude numbers.

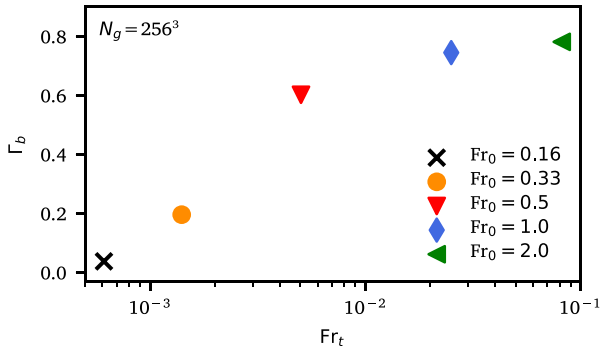

Fig. 16. Relation of flux coefficient of the bulk Γ_b with time-integrated turbulent Froude number Fr_t for different initial Froude numbers.

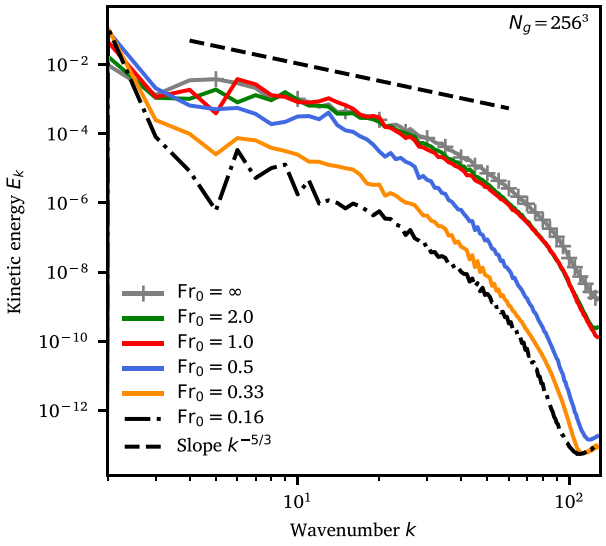

Fig. 17. Kinetic energy over wavenumber at $t = 15$ for the same Froude numbers as in Fig. 13. The dashed line shows the slope $k^{-5/3}$.

Froude numbers on the horizontal velocity $\sqrt{u_x^2 + u_y^2}$. It is apparent that the strong stratification triggered by low Froude numbers, such as $\mathrm{Fr}_0 = 0.33$, maintains the original flow structure.

3.5. Comparison of forcing schemes

To compare the forcing schemes by Shan–Chen, Kupershtokh, and Guo, the dissipation of the potential energy ε_p was measured with these forcing schemes. Fig. 19 indicates that the choice of the forcing model is not as decisive as the stencil configuration for the flow explored in this article, for all three forcing schemes nearly equally reproduced the dissipation of the turbulent potential energy ε_p, except for a minor deviation of the Guo scheme around $t = 30$.

3.6. Comparison of collision models BGK and KBC

Last, the BGK and KBC collision models were compared for the stratified simulations at $N_g = 64^3$ and $N_g = 128^3$. For this comparison, the Kupershtokh forcing scheme was used, since its forcing term can be used seamlessly with most collision models. The stencil was set to D3Q27x7. The results are depicted in Fig. 20, where it can be seen that the KBC collision model at $N_g = 64^3$ clearly stabilizes the simulations. This contrasts with the BGK model, which is unstable at this resolution and configuration. However, the KBC model fails to predict the dissipation peak and overestimates the dissipation beginning from $t = 20$.

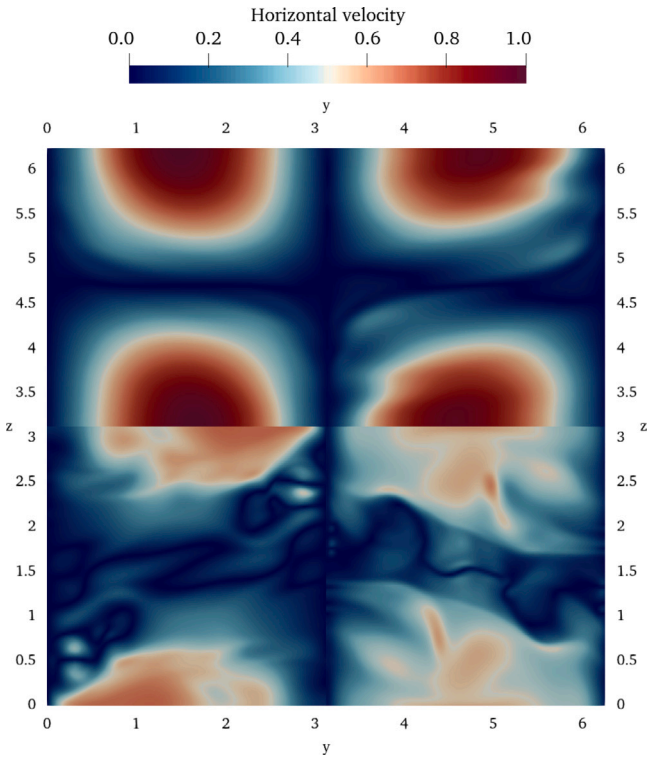

Fig. 18. Horizontal velocity of the y-z plane at $x = 0$ and $t = 15$ for different Froude numbers. Upper left quadrant: $\mathrm{Fr}_0 = 0.33$, Upper right: $\mathrm{Fr}_0 = 0.5$, Lower left: $\mathrm{Fr}_0 = 1.0$, Lower right: $\mathrm{Fr}_0 = 2.0$.

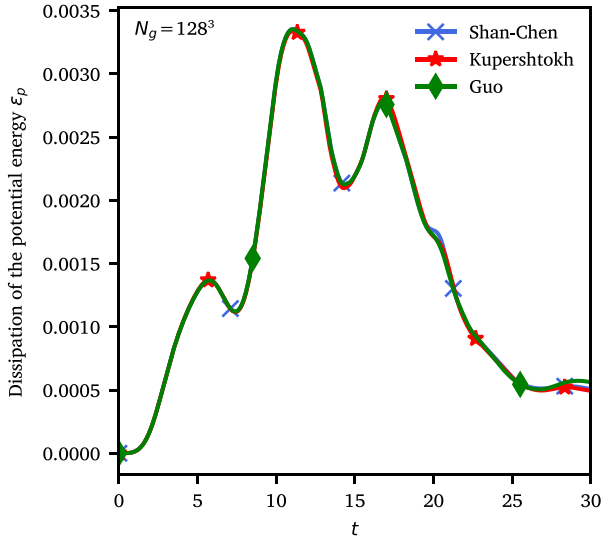

Fig. 19. Comparison of ε_p for the forcing schemes by Shan and Chen, Kupershtokh et al., and Guo et al..

When increasing the resolution to $N_g = 128^3$, the prediction of the peak is significantly better. On the flip side, the deviation from the reference is larger than the deviation of the BGK model at the same resolution. This indicates that the KBC model introduces a significant amount of numerical dissipation into the simulation. Still, to improve the stability of the simulation, the KBC collision model remains one option, but at the cost of degrading accuracy.

4. Conclusion

We have shown that the LBM can accurately capture the evolution of turbulence and mixing in a stratified Taylor–Green vortex. The kinetic, and potential energy, the dissipation rates and different Froude numbers were explored. The overall agreement of the lattice Boltzmann simulations with a previous study [30] is excellent. It turned out that the combination of a D3Q27 stencil for the momentum equation combined with a D3Q7 for the advection–diffusion equation of the density variation led to the best results regarding total dissipation. Using a larger stencil for the second distribution function results in matching the dissipation rates less well, but also rendered the simulations stabler. By contrast, altering the forcing scheme left the simulation results nearly unchanged. In addition, using an alternative collision model, such as the KBC entropic multi-relaxation time model, proved as an option to stabilize underresolved simulations. For slightly underresolved flow, using a stencil with more than seven velocities for the second distribution function can be an option, though.

To sum up, the present study demonstrated that the LBM has the potential to accurately simulate stratified homogeneous turbulence given the appropriate choice of grid resolution and discretization stencils. Not only the LBM captures the evolution of large-scale kinetic and potential energy, it also can capture the amount of turbulent mixing, which has important applications in environmental flows. In future work, it is of interest to explore the performance of LBM in more realistic atmospheric/oceanic flows in which the physics are influenced by complex velocity shear (e.g., due to wind or ocean currents), topography (i.e, effects due to wall-bounded turbulence), rotation, surface and internal waves.

CRediT authorship contribution statement

Dominik Wilde: Conceptualization, Methodology, Software, Validation, Investigation, Writing – original draft. **Sheel Nidhan:** Conceptualization, Validation, Investigation, Writing – review & editing. **Hieu T. Pham:** Conceptualization, Validation, Investigation, Writing – review & editing. **Holger Foysi:** Investigation, Resources, Writing – review & editing. **Dirk Reith:** Investigation, Validation, Writing – review & editing, Funding acquisition. **Sutanu Sarkar:** Conceptualization, Methodology, Investigation, Resources, Writing – review & editing, Supervision.

Declaration of competing interest

The authors declare that they have no known competing financial interests or personal relationships that could have appeared to influence the work reported in this paper.

Data availability

Data will be made available on request.

Acknowledgments

D.W. is supported by German Research Foundation (DFG) project FO 674/17-1. D.W. and his family would like to thank DAAD (German Academic Exchange Service) for partially covering the travel costs, child care expenses, and living costs during a research stay at UC San Diego.

Appendix. Stencils of the lattice Boltzmann method

See Table A.1.

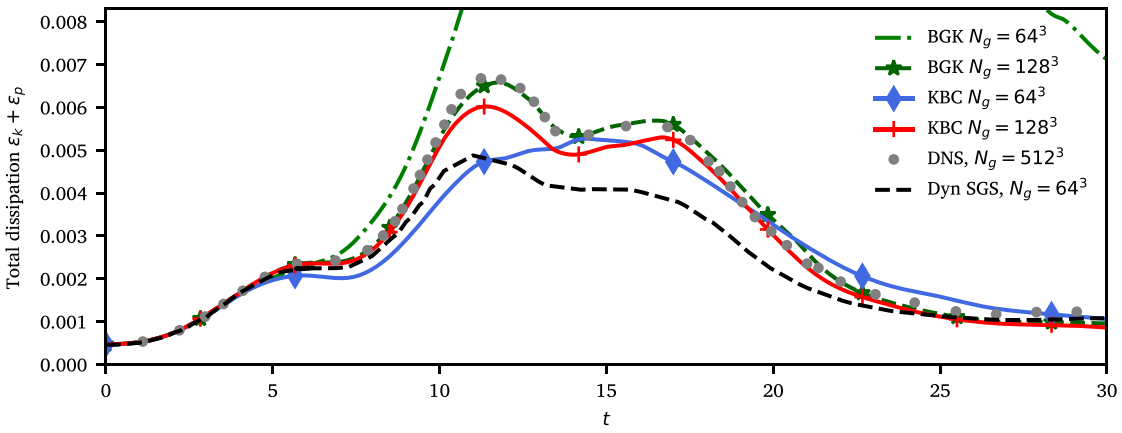

Fig. 20. Comparison of the BGK and KBC collision model in terms of the resolved total dissipation. DNS and Dynamic Smagorinsky model (Dyn SGS) by Jadhav and Chandy [30].

Table A.1
Compilation of the stencils D3Q7, D3Q19, and D3Q27.

Stencil	Lattice speed of sound c_s	Index i	Weight w_i	Discrete velocity $\boldsymbol{c}_i$
D3Q7	$1/2$	0	$1/4$	$(0,0,0)$
		$1,\ldots,6$	$1/8$	$(\pm1,0,0),(0,\pm1,0),(0,0,\pm1)$,
D3Q19	$1/\sqrt{3}$	0	$1/3$	$(0,0,0)$
		$1,\ldots,6$	$1/18$	$(\pm1,0,0),(0,\pm1,0),(0,0,\pm1)$,
		$7,\ldots,18$	$1/36$	$(\pm1,\pm1,0),(\pm1,0,\pm1),(0,\pm1,\pm1)$
D3Q27	$1/\sqrt{3}$	0	$8/27$	$(0,0,0)$
		$1,\ldots,6$	$2/27$	$(\pm1,0,0),(0,\pm1,0),(0,0,\pm1)$,
		$7,\ldots,18$	$1/54$	$(\pm1,\pm1,0),(\pm1,0,\pm1),(0,\pm1,\pm1)$
		$19,\ldots,26$	$1/216$	$(\pm1,\pm1,\pm1)$

References

[1] Caulfield CP. Layering, instabilities, and mixing in turbulent stratified flows. Annu Rev Fluid Mech 2021;53:113–45. http://dx.doi.org/10.1146/annurev-fluid-042320-100458.

[2] Ross AN, Arnold S, Vosper SB, Mobbs S, Dixon N, Robins AG. A comparison of wind-tunnel experiments and numerical simulations of neutral and stratified flow over a hill. Boundary-Layer Meteorol 2004;113(3):427–59. http://dx.doi.org/10.1023/B:BOUN.0000045499.18839.7d.

[3] McNamara GR, Zanetti G. Use of the Boltzmann equation to simulate lattice-gas automata. Phys Rev Lett 1988;61(20):2332–5. http://dx.doi.org/10.1103/PhysRevLett.61.2332.

[4] Lallemand P, Luo LS, Krafczyk M, Yong WA. The lattice Boltzmann method for nearly incompressible flows. J Comput Phys 2021;431:109713. http://dx.doi.org/10.1016/j.jcp.2020.109713.

[5] Krüger T, Kusumaatmaja H, Kuzmin A, Shardt O, Silva G, Viggen EM. The Lattice Boltzmann Method: Principles and Practice. Springer; 2017, http://dx.doi.org/10.1007/978-3-319-44649-3, arXiv:arXiv:1011.1669v3.

[6] Krause MJ, Kummerländer A, Avis SJ, Kusumaatmaja H, Dapelo D, Klemens F, Gaedtke M, Hafen N, Mink A, Trunk R, Marquardt JE, Maier ML, Haussmann M, Simonis S. OpenLB—Open source lattice Boltzmann code. Comput Math Appl 2021;81:258–88. http://dx.doi.org/10.1016/j.camwa.2020.04.033.

[7] Wichmann K-R, Kronbichler M, Löhner R, Wall WA. A runtime based comparison of highly tuned lattice Boltzmann and finite difference solvers. Int J High Perform Comput Appl 2021;35(4):370–90.

[8] Dorschner B, Bösch F, Chikatamarla SS, Boulouchos K, Karlin IV. Entropic multi-relaxation time lattice Boltzmann model for complex flows. J Fluid Mech 2016;801(September):623–51. http://dx.doi.org/10.1017/jfm.2016.448.

[9] Guo Z, Shi B, Zheng C. A coupled lattice BGK model for the Boussinesq equations. Internat J Numer Methods Fluids 2002;39(4):325–42. http://dx.doi.org/10.1002/fld.337.

[10] Scagliarini A, Biferale L, Sbragaglia M, Sugiyama K, Toschi F. Lattice Boltzmann methods for thermal flows: Continuum limit and applications to compressible Rayleigh-Taylor systems. Phys Fluids 2010;22(5):1–21. http://dx.doi.org/10.1063/1.3392774, arXiv:1005.3639.

[11] Shan X. Simulation of Rayleigh-Bénard convection using a lattice Boltzmann method. Phys Rev E 1997;55(3):2780–8. http://dx.doi.org/10.1103/PhysRevE.55.2780, arXiv:9612001v1.

[12] Lohse D, Toschi F. Ultimate state of thermal convection. Phys Rev Lett 2003;90(3):034502.

[13] Calzavarini E, Toschi F, Tripiccione R. Evidences of Bolgiano-Obhukhov scaling in three-dimensional Rayleigh-Bénard convection. Phys Rev E 2002;66(1):016304.

[14] Kao PH, Yang RJ. Simulating oscillatory flows in Rayleigh-Bénard convection using the lattice Boltzmann method. Int J Heat Mass Transfer 2007;50(17–18):3315–28. http://dx.doi.org/10.1016/j.ijheatmasstransfer.2007.01.035.

[15] Frapolli N, Chikatamarla SS, Karlin IV. Entropic lattice Boltzmann simulation of thermal convective turbulence. Comput & Fluids 2018;175(July):2–19. http://dx.doi.org/10.1016/j.compfluid.2018.08.021.

[16] Biferale L, Mantovani F, Sbragaglia M, Scagliarini A, Toschi F, Tripiccione R. Second-order closure in stratified turbulence: Simulations and modeling of bulk and entrainment regions. Phys Rev E 2011;84(1):016305.

[17] Wang Y, MacCall BT, Hocut CM, Zeng X, Fernando HJ. Simulation of stratified flows over a ridge using a lattice Boltzmann model. Environ Fluid Mech 2020;20(5):1333–55. http://dx.doi.org/10.1007/s10652-018-9599-3.

[18] Feng Y, Boivin P, Jacob J, Sagaut P. Hybrid recursive regularized lattice Boltzmann simulation of humid air with application to meteorological flows. Phys Rev E 2019;100(2):23304. http://dx.doi.org/10.1103/PhysRevE.100.023304.

[19] Dapelo D, Simonis S, Krause MJ, Bridgeman J. Lattice-Boltzmann coupled models for advection–diffusion flow on a wide range of Péclet numbers. J Comput Sci 2021;51(March):101363. http://dx.doi.org/10.1016/j.jocs.2021.101363.

[20] Taylor GI, Green AE. Mechanism of the production of small eddies from large ones. Proc R Soc Lond A Math Phys Sci 1937;158(895):499–521.

[21] DeBonis J. Solutions of the Taylor-Green vortex problem using high-resolution explicit finite difference methods. In: 51st AIAA aerospace sciences meeting including the new horizons forum and aerospace exposition. Reston, Virigina: American Institute of Aeronautics and Astronautics; 2013, http://dx.doi.org/10.2514/6.2013-382.

[22] Drikakis D, Fureby C, Grinstein FF, Youngs D. Simulation of transition and turbulence decay in the Taylor-Green vortex. J Turbul 2007;8:1–12. http://dx.doi.org/10.1080/14685240701250289.

[23] Bull JR, Jameson A. Simulation of the Taylor-Green vortex using high-order flux reconstruction schemes. AIAA J 2015;53(9):2750–61. http://dx.doi.org/10.2514/1.J053766.

[24] Krämer A, Wilde D, Küllmer K, Reith D, Foysi H. Pseudoentropic derivation of the regularized lattice Boltzmann method. Phys Rev E 2019;100(2):023302. http://dx.doi.org/10.1103/PhysRevE.100.023302.

[25] Peng N, Yang Y. Effects of the Mach number on the evolution of vortex-surface fields in compressible Taylor-Green flows. Phys Rev Fluids 2018;3(1):1–21. http://dx.doi.org/10.1103/PhysRevFluids.3.013401.

[26] Lusher DJ, Sandham ND. Assessment of low-dissipative shock-capturing schemes for the compressible taylor–green vortex. AIAA J 2021;59(2):533–45. http://dx.doi.org/10.2514/1.J059672.

[27] Wilde D, Krämer A, Reith D, Foysi H. High-order semi-Lagrangian kinetic scheme for compressible turbulence. Phys Rev E 2021;104(2):1–15. http://dx.doi.org/10.1103/PhysRevE.104.025301, arXiv:2012.05537.

[28] Remmler S, Hickel S. Direct and large eddy simulation of stratified turbulence. Int J Heat Fluid Flow 2012;35:13–24. http://dx.doi.org/10.1016/j.ijheatfluidflow.2012.03.009.

[29] Rahimi A, Chandy AJ. Direct numerical simulations of non-helical and helical stratified turbulent flows. J Turbul 2016;17(1):1–29. http://dx.doi.org/10.1080/14685248.2015.1078469.

[30] Jadhav K, Chandy AJ. Assessment of SGS models for large eddy simulation (LES) of a stratified Taylor–Green vortex. Flow Turbul Combust 2021;106(1):37–60. http://dx.doi.org/10.1007/s10494-020-00175-5.

[31] Bhatnagar PL, Gross EP, Krook M. A model for collision processes in gases. I. Small amplitude processes in charged and neutral one-component systems. Phys Rev 1954;94(3):511–25. http://dx.doi.org/10.1103/PhysRev.94.511.

[32] Wilde D, Krämer A, Küllmer K, Foysi H, Reith D. Multistep lattice Boltzmann methods: Theory and applications. Internat J Numer Methods Fluids 2019;90(3):156–69. http://dx.doi.org/10.1002/fld.4716.

[33] Shan X, Chen H. Lattice Boltzmann model for simulating flows with multiple phases and components. Phys Rev E 1993;47:1815–9. http://dx.doi.org/10.1103/PhysRevE.47.1815.

[34] Kupershtokh AL, Medvedev DA, Karpov DI. On equations of state in a lattice Boltzmann method. Comput Math Appl 2009;58(5):965–74. http://dx.doi.org/10.1016/j.camwa.2009.02.024.

[35] Guo Z, Zheng C, Shi B. Discrete lattice effects on the forcing term in the lattice Boltzmann method. Phys Rev E 2002;65(4):6. http://dx.doi.org/10.1103/PhysRevE.65.046308.

[36] Huang H, Krafczyk M, Lu X. Forcing term in single-phase and Shan-Chen-type multiphase lattice Boltzmann models. Phys Rev E 2011;84(4). http://dx.doi.org/10.1103/PhysRevE.84.046710.

[37] Shan X, Yuan XF, Chen H. Kinetic theory representation of hydrodynamics: A way beyond the Navier-Stokes equation. J Fluid Mech 2006;550(-1):413–41. http://dx.doi.org/10.1017/S0022112005008153.

[38] Wilde D, Krämer A, Bedrunka M, Reith D, Foysi H. Cubature rules for weakly and fully compressible off-lattice Boltzmann methods. J Comput Sci 2021;51(April):101355. http://dx.doi.org/10.1016/j.jocs.2021.101355, arXiv:2101.03982.

[39] Sterling JD, Chen S. Stability Analysis of Lattice Boltzmann Methods. J Comput Phys 1996;123(1):196–206. http://dx.doi.org/10.1006/jcph.1996.0016.

[40] Lallemand P, Luo LS. Theory of the lattice Boltzmann method: Dispersion, dissipation, isotropy, Galilean invariance, and stability. Phys Rev E 2000;61(6):6546–62. http://dx.doi.org/10.1103/PhysRevE.61.6546.

[41] Karlin IV, Bösch F, Chikatamarla SS. Gibbs' principle for the lattice-kinetic theory of fluid dynamics. Phys Rev E 2014;90(3):31302. http://dx.doi.org/10.1103/PhysRevE.90.031302.

[42] Bösch F, Chikatamarla SS, Karlin IV. Entropic multirelaxation lattice Boltzmann models for turbulent flows. Phys Rev E 2015;92(4):1–15. http://dx.doi.org/10.1103/PhysRevE.92.043309, arXiv:1507.02518.

[43] Morrison HE, Leder A. Sediment transport in turbulent flows with the lattice Boltzmann method. Comput & Fluids 2018;172:340–51. http://dx.doi.org/10.1016/j.compfluid.2018.04.015.

[44] Brachet ME, Meiron DI, Orszag SA, Nickel BG, Morf RH, Frisch U. Small-scale structure of the Taylor–Green vortex. J Fluid Mech 1983;130(-1):411. http://dx.doi.org/10.1017/S0022112083001159.

[45] Fritsch RA, Bedrunka MC, Krämer A, Wilde D, Wismüller R, Reith D, Foysi H. Efficient CUDA Implementation of the Lattice Boltzmann method in a PyTorch-based Open Source Framework. 2023, in preparation.

[46] Osborn T. Estimates of the local rate of vertical diffusion from dissipation measurements. J Phys Oceanogr 1980;10(1):83–9.

[47] Mashayek A, Caulfield CP, Peltier WR. Time-dependent, non-monotonic mixing in stratified turbulent shear flows: Implications for oceanographic estimates of buoyancy flux. J Fluid Mech 2013;736(December):570–93. http://dx.doi.org/10.1017/jfm.2013.551.

[48] VanDine A, Pham HT, Sarkar S. Turbulent shear layers in a uniformly stratified background: DNS at high Reynolds number. J Fluid Mech 2021;916:1–35. http://dx.doi.org/10.1017/jfm.2021.212.

[49] Onuki Y, Joubaud S, Dauxois T. Simulating turbulent mixing caused by local instability of internal gravity waves. J Fluid Mech 2021;915:1–14. http://dx.doi.org/10.1017/jfm.2021.119.